Earth and Planetary Science Letters 578 (2022) 117288

Contents lists available at ScienceDirect

Earth and Planetary Science Letters

www.elsevier.com/locate/epsl

Lateral coexistence of ductile and brittle deformation shapes magma-poor distal margins: An example from the West Iberia-Newfoundland margins

Zhonglan Liu [a,*], Marta Pérez-Gussinyé [a,*], Lars Rüpke [b], Iskander A. Muldashev [a], Timothy A. Minshull [c], Gaye Bayrakci [d]

[a] MARUM, Center for Marine Environmental Sciences, University of Bremen, 28359 Bremen, Germany
[b] GEOMAR, Helmholtz Centre for Ocean Research Kiel, Marine Geodynamics, 24148 Kiel, Germany
[c] University of Southampton, School of Ocean and Earth Science, National Oceanography Centre Southampton, Southampton SO14 3ZH, UK
[d] National Oceanography Centre, Waterfront Campus, Southampton, SO14 3ZH, UK

ARTICLE INFO

Article history:
Received 23 August 2021
Received in revised form 25 October 2021
Accepted 5 November 2021
Available online 24 November 2021
Editor: R. Bendick

Keywords:
magma-poor margins
deformation patterns
detachment faults
geodynamical modeling

ABSTRACT

A long-standing problem in solid Earth science is to understand how low-angle normal faults form, their role in the development of tectonic asymmetry of conjugate margins, and how they relate to mantle hydration during continental breakup. The latter requires water to reach the mantle through active brittle faults, but low angle slip on faults is mechanically difficult. Here, we incorporate observations from high-resolution multichannel seismic data along the West Iberia-Newfoundland margins into a 2D forward thermo-mechanical model to understand the relationship between evolving rift asymmetry, detachment tectonics, and mantle hydration. We show that, during extreme extension, slip on active faults bifurcates at depth into brittle and ductile deformation branches, as a result of the cooling of the faults' footwall and heating of their hangingwall. The brittle deformation penetrates the Moho and leads to mantle hydration, while ductile deformation occurs in localized shear zones and leads to the formation of detachment-like structures in the distal margin sections. Such structures, as for example '*S*' in the West Iberia-Newfoundland margins, are thus composed of several shear zones, active at low-angles, ~25°-20°, and merging with the Moho at depth. The final sub-horizontal geometry of these structures is the result of subsequent back-rotation of these shear zones by new oceanward faults. Our results reproduce remarkably well the final sedimentary, fault, crustal architecture, and serpentinisation pattern observed at the West Iberia-Newfoundland margins. However, they challenge widely accepted ideas that such detachment-like structures formed by brittle processes, separate crust from mantle and caused conjugate margin asymmetry. Our model provides a quantitative framework to study hydrothermal systems related to serpentinization during extreme extension, their associated hydrogen, methane production, and the chemosynthetic life they sustain.

1. Introduction

Magma-poor rifting is a fundamental extension mode in nature, in which hydrothermal circulation, mantle hydration, and intense element exchange between solid Earth and ocean occur, shaping the carbon cycle and deep life in the oceans (Bayrakci et al., 2016; Albers et al., 2021). In the North Atlantic, magma-poor rifted margins share similar architectural patterns and tectonic evolution (Péron-Pinvidic et al., 2013; Reston, 2009, Pérez-Gussinyé and Reston, 2001) (Fig. 1a). They often display an asymmetric conjugate structure, with a narrow margin where the crust thins abruptly and a wider margin exhibiting much smoother crustal thinning (Hopper et al., 2004; Ranero and Pérez-Gussinyé, 2010). The wide conjugate is characterized by large faults, which become progressively listric oceanwards, and overlie characteristic bands of strong sub-horizontal reflectivity in the lower crust (Osmundsen and Péron-Pinvidic, 2018; Pérez-Gussinyé et al., 2003). In the West Iberia margin, and elsewhere (Blaich et al., 2011; Osmundsen and Péron-Pinvidic, 2018), progressive extension culminates with the formation of a large low-angle detachment-like structure in

* Corresponding authors.
E-mail addresses: zhonglan@uni-bremen.de (Z. Liu), gussinye@uni-bremen.de (M. Pérez-Gussinyé).

https://doi.org/10.1016/j.epsl.2021.117288
0012-821X/

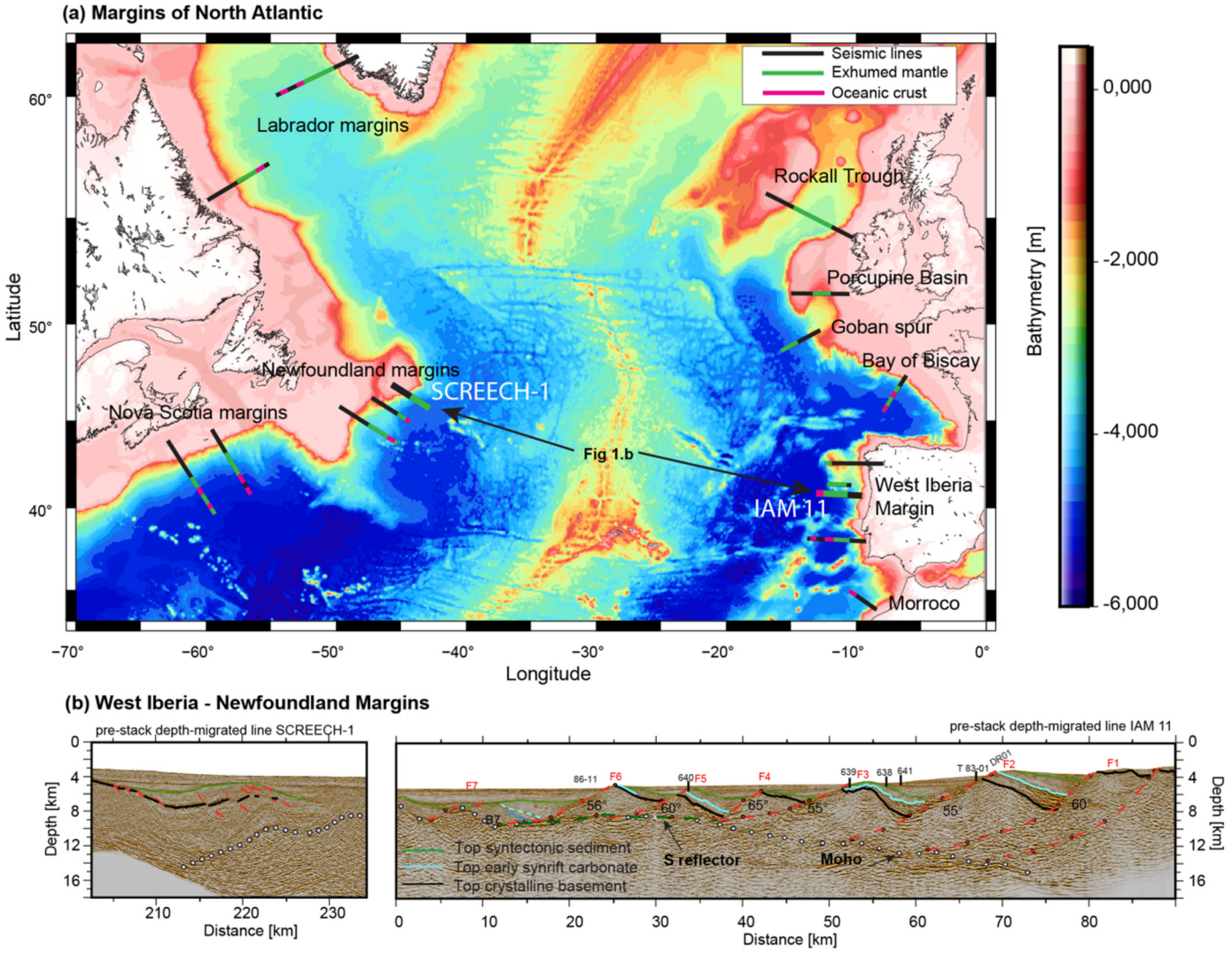

Fig. 1. Observations on magma-poor margins. (a) Margins of North Atlantic where exhumed and serpentinised mantle has been interpreted based on multichannel and wide-angle seismic data (for references see Reston, 2009). **(b)** Interpreted SCREECH1- IAM11 seismic section on the West Iberia (WIM)-Newfoundland (NF) margins (Ranero and Pérez-Gussinyé, 2010) shows a markedly asymmetric conjugate margin, with a narrow margin (NF) where the crust thins sharply and a wider margin (WIM) that displays much smoother crustal thinning. The WIM margin is characterized by a large, sub-horizontal detachment, the S reflector. The initial fault angles were adopted from Ranero and Pérez-Gussinyé (2010) and are used in kinematic-dynamic modeling. ODP sites 637-641, dredge T83-01 and dive 86-11 were used for calibrated stratigraphic interpretation by Boillot et al. (1987). (For interpretation of the colors in the figure(s), the reader is referred to the web version of this article.)

the distal margin (Ranero and Pérez-Gussinyé, 2010; Reston, 1996; Schuba et al., 2018; Lymer et al., 2019) (Fig. 1b).

The mechanisms of formation of low-angle detachments at magma-poor margins and their role in margin asymmetry formation are contentious. Detachments may slip as a single entity at low-angle, which requires very low friction coefficients, local high pore pressure, and/or initial stress rotation (when slip occurs in the brittle field, e.g., Axen and Karner, 2004; Lister et al., 1991), or may be formed by the deep segments of faults active at high angles, which were subsequently rotated to low-angles by new oceanward faults (Ranero and Pérez-Gussinyé, 2010), similar as in the rolling hinge model (Buck, 1988; Sandiford et al., 2021). Three-dimensional multichannel seismic data from the so-called *S* detachment of the distal West Iberia margin, show coherent corrugations continuing from the detachment surface to the overlying faults (Lymer et al., 2019). Stratigraphic analysis indicates that the detachment is a composite structure formed by the deep segments of overlying sequentially active, oceanward younging faults (Lymer et al., 2019). However, interpretation from the geometrical relationships between the detachment and overlying sediments convincingly shows that slip on the detachment occurred at low angles, 20–25° (Lymer et al., 2019). Hence, the formation of the detachment at distal magma-poor margin matches neither the rolling-hinge model, which suggests active slip on the detachment occurs at high-angle (Buck, 1988), nor that of a single detachment slipping simultaneously at a low angle (Axen and Karner, 2004; Lister et al., 1991).

In the last two decades, studies have suggested those detachments in the magma-poor margins distal sections form completely in the brittle field without intervention of ductile deformation (Pérez-Gussinyé and Reston, 2001, Lymer et al., 2019). Their formation is related to whole crustal embrittlement allowing the formation of crustal-scale faults, through which the water required for serpentinisation reaches the mantle (Pérez-Gussinyé and Reston, 2001). In this conceptual model, active low-angle slip on the brittle detachment is facilitated by the large serpentinization related weakening, plus high local pore pressures (Pérez-Gussinyé and Reston, 2001). Lymer et al. (2019) have expanded this idea and suggested that those detachments cause the overall asymmetry observed at these margins.

However, multichannel seismic reflection data along the West Iberia margin show that the structural tectonic asymmetry starts in areas located much further landward than that of the detachment, suggesting the detachment could not generate the large-scale asymmetry observed (Fig. 1b). Kinematic reconstructions of the West Iberia-Newfoundland margins indicate that the asymmetry in faulting pattern and crustal thinning can be well reproduced by the emergence of an oceanward dipping and younging fault array which is sequential in time and is active only in the future wide margin (Ranero and Pérez-Gussinyé, 2010). According to this interpretation, the sequential fault array laterally migrates from the wide towards the future narrow margin. Brune et al. (2014) suggested the migration of deformation is maintained by a weak and narrow lower crust channel at the crust's base. However, as pointed out by Lymer et al. (2019), the concept of asymmetry formation being promoted by the existence of such a weak lower crustal channel, conflicts with the existence of mantle hydration inferred from seismic data beneath the S detachment (Bayrakci et al., 2016), which requires whole crustal embrittlement to allow water to reach the mantle and hydrate it (Pérez-Gussinyé and Reston, 2001).

In this work we use a newly developed 2D numerical modelling technique, Kinedyn (Muldashev et al., 2021), to show a possible way to reconcile the ideas that asymmetric margin formation requires a weak and narrow lower crustal channel (Brune et al., 2014), and the well-accepted assumption that serpentinisation beneath the thinned crust requires whole crustal embrittlement (Pérez-Gussinyé and Reston, 2001). We find that during extreme extension the rocks in the footwalls of active faults cool, while those in their hangingwalls heat. Cooling in the faults' footwalls ultimately leads to brittle deformation and mantle hydration. However, heating in the faults' hangingwalls leads to ductile shearing at low-angle and formation of detachment-like structures in the distal margin sections such as *S*. Although the focus is on the well-studied West Iberia-Newfoundland margins, the resulting concepts are applicable to other magma-poor margins worldwide, and useful for the study of hydrothermal systems and their corresponding element fluxes during extreme extension.

2. Methods

2.1. Modeling philosophy and assumptions

Over the past three decades, geodynamic modelling has brought huge advances in our understanding of the mechanisms of extension at rifted margins (e.g., Buck, 1991; Lavier and Manatschal, 2006; Huismans and Beaumont, 2011; Brune et al., 2014; Naliboff et al., 2017; Ros et al., 2017; Pérez-Gussinyé et al., 2020; Peron-Pinvidic and Naliboff, 2020). However, the difficulty in matching model results with seismic sections at fault-block scale, has left model-data comparison at the level of large-scale features, such as degree of margin asymmetry, abruptness of crustal thinning, margin width etc. Thus, detailed reconstruction of rifted margins, able to reproduce the fault-block scale tectonic features along a seismic multichannel reflection line is currently not possible with purely forward models. A way to reconcile the forward model with the available observations is to fuse both in some mechanistic way. This should, for example, lead to improved matching of temperature and deformation field evolution, in turn leading to more accurate assessments of processes occurring at fault-block scales, such as fluid-rock interactions and their corresponding element exchange (Albers et al., 2021).

A problem of fusing data and models arises in scientific areas that enjoy a wealth of data and use costly models. In the geophysical community this fusion is commonly referred to as inversion and data assimilation, whose aim is to find the best estimate of the state of the geophysical system by combining information from the observations and from the numerical and theoretical knowledge of the underlying governing dynamical laws. Most known assimilation methods stem from Bayes' theorem (Lorenc, 1986), and each is made practical by making approximations (Bannister, 2017). In the field of geodynamics, there have been a few inversion attempts, where field observations have been used to estimate geodynamic model parameters and/or initial conditions. For example, Baumann and Kaus (2015) use present day observations of topography, gravity, and surface velocities from the India-Asia collision zone to invert for creep-law parameters that control the rheology of the lithosphere. The intention of their analysis is to constrain a set of rheological parameters that best fit present day topography, gravity and velocity at large spatial scales (i.e. more than $\sim$100 km of wavelength). Also, Reuber et al. (2018) use geodynamic inversion in the Yellowstone magmatic system to constrain the viscosities that best reproduce the observed GPS velocities. In both geodynamic inversions, the model geometry is assumed to be known at the start of the inversion approach, and the geodynamic models are ran for $\sim 10^4$ years to bring the model to a stable situation where the model outputs can be compared to the geophysical observations. For longer temporal scales, data assimilation has been used to reconstruct the evolution of mantle flow by updating the model when observational constraints are available (e.g. plate motion history and seafloor ages, Zhou and Liu, 2017). However, inversion/data assimilation using geodynamic models generally focuses on relatively large spatial-scale features (>$\sim$100 km), sometimes even passing low-frequency filters to both model and observations as a mechanism to stabilise the problem (e.g., Baumann and Kaus, 2015).

Our interest, instead, is on reconstructing not only the large-scale but also the smaller, fault-block scale deformation during rifting on time scales of tens of millions of years. The small spatial scale along with the long temporal scales results in a much stronger non-linear relation between both the model parameters and initial conditions with observations than in the abovementioned studies. In addition there is a natural heterogeneity in crustal and mantle composition that will prevent any geodynamic model from accurately reproducing a specific tectonic structure at fault-block scale. Also, as a fault is initiated, its feedback on the system is itself nonlinear. Thus the only way to reconstruct the tectonic evolution of rifted margins at fault-block scale, is to keep the model on track through a sequential assimilation scheme in which the model is nudged towards the observations through time.

Our approach uses as observations fault locations, initial angle, offsets and times of fault activity interpreted from a given multichannel seismic profile and atempts to fit the tectonic structure, i.e. crustal thickness, basement topography at fault-block scale. The updating of system evolution is done by introducing the interpreted faults as weak planes in the model upper crust, at the times interpreted from the seismic section until the observed fault offset is reached. Our solver uses a Lagrangian approach where the mesh is deformed in time. Mesh adaptation through time includes automated remeshing. This remeshing hampers the application of straightforward statistical assimilation approaches (such as the ensemble Kalman filter or fully non-linear approaches such as the particle filters), as a different state space dimension exists across the members of the ensemble. Methods for adaptive (Lagrangian) moving mesh assimilation have been recently discussed (e.g. Aydoğdu et al., 2019), and could potentially be used. Still, an additional challenge is that the observations themselves do not lie in a fixed Eulerian referential framework, as they need to be taken from the present-day seismic snapshot, and placed backward in time, taking previous faults as a spatial reference framework. All this, along with the complexity of defining a metric for the model-data misfit at the local fault-block scale, makes our assimilation

problem a very difficult one. Our practical stance here is to conduct a heuristic nudging, where expertises in both model dynamics and seismic section reconstruction take the place of automated assimilation steps.

Our technique allows us to guide the model to simulate an interpretation of a seismic line. Thus, we test whether an interpretation for margin evolution, reproduces its tectonic structure, and simultaneously investigate the consequences of such an interpretation for the dynamics of rifting. Although a tectonic interpretation is non-unique, Kinedyn allows to test whether it is compatible with the observed seismic structure and the physics of rock deformation. The specifics of the approach follow below, and are further detailed in Muldashev et al. (2021).

2.2. General modeling strategy

KineDyn, can work in a forward dynamic mode, or in a mode called "kinematic-dynamic", where initial fault locations and angles obtained from observations are imposed as weak planes at selected times during the forward model run (Muldashev et al., 2021). In this way, we guide the upper crustal strain localization during extension periods where faults are clearly observed in seismic sections and let the model evolve forward in time dynamically, where we have no observational constraints on fault.

During the dynamic simulation stage, the code works as for a standard thermo-mechanical, elasto-visco-plastic mode (see Appendix) that is described in detail elsewhere (Muldashev et al., 2021). In the kinematic-dynamic simulation stage, we include kinematic faults by introducing weak planes. Unless noted in the text, we assume that the width of weak planes is 200 m and that its depth reaches the base of the upper crust. The effect of strain weakening is assumed to be maximum along weak planes so that the cohesion and friction angle of weak planes reach minimum values and are equal to 10 MPa and 15°, respectively. In Section 2.4, we show that widths and strength of weak planes have negligible effect on the results. Plasticity is prohibited in the upper crust outside of these weak planes, so extension of the model results in slip on the prescribed faults. The included weak planes are not required to deform in a plastic way, so that, they will deform in the plastic or ductile fields according to the Drucker-Prager yield equation (Appendix). It is important to note that the upper crust outside those planes can still deform visco-elastically and that, in addition, deformation in the rest of the model, i.e., lower crust and mantle, is visco-elasto-plastic in response to the imposed extension velocities on the sides, and in the presence of the introduced weakness planes (Muldashev et al., 2021).

Each fault is assigned a final offset that is estimated from the given seismic section. When the simulated fault reaches this offset, it becomes deactivated and further plastic deformation will be prohibited along it. The location of a new fault is only determined when the slip on the previous fault is completed. This allows the fault spacing measured along the seismic profile to be exactly incorporated into the model, avoiding the effects of horizontal stretching from early simulation stages. The rate of slip on each weak plane is not imposed but is affected by the stress state and the location of weak planes.

It is important to note that, even in the "kinematic-dynamic mode", only the initial fault angle, location and final offset are prescribed. Subsequently, the model is allowed to run dynamically in time, so that the final fault angle, basement, sedimentary geometries, and crustal thickness result from dynamic feedbacks between ductile and brittle deformation. In this way, the final modelled section results from a process in which the interpretations of a seismic section (in terms of the time sequence of the observed faults), and the key parameters that affect dynamic model evolution, such as initial rheology and geothermal gradients, are iteratively modified, until they coherently explain the architecture observed along the seismic profile.

2.3. Model set up

In this study, we aim to understand the detailed spatio-temporal evolution of deformation during extension of the West Iberia-Newfoundland margins by obtaining a modeled section that reproduces the tectonic architecture along the conjugate seismic multichannel profiles IAM 11- Screech1 (Fig. 1b, Hopper et al., 2004 and Ranero and Pérez-Gussinyé, 2010). The seismic profiles only provide constraints on the period where crust thinned from about 18 km to zero. Hence, we start our model in dynamic mode. Once our simulation has reached a minimum crustal thickness of 18 kilometers, which is equal to the crustal thickness of the eastern side of line of IAM 11, we start to run the model in kinematic-dynamic mode.

We assume some modelling parameters are known and chosen as follows (Fig. 2 and Table S1): 1) The initial depth of the lithosphere-asthenosphere boundary, has a value of 105 km, which agrees with the estimated present-day range of values for the Iberian Peninsula (Artemieva, 2006). The thermal gradient between the surface and the base of the lithosphere is then calculated based on the lithosphere's age and the radiogenic heat production of crustal layers. 2) The initial crustal thickness is set to 33 km, supported by seismic data onshore Iberia (Zelt et al., 2003). Seismic studies in less extended areas nearby show that upper crustal thickness is about 80% of lower crustal thickness (Pérez-Gussinyé et al., 2003). Based on this, the upper crust is set to 15 km thick, while the lower crust extends from 15 km to 33 km depth. 3) The full extension rate in our model is set to 8 mm/a according to estimates of extension rate at the west Iberia margin, which show that the extension velocity increases from 4 mm/a during an early stage of rifting to less than 10 mm/a during the mantle exhumation stage (Sibuet et al., 2007).

The fault kinematics are similar to those of Ranero and Pérez-Gussinyé (2010) which were constrained by manually reconstructing the conjugate depth migrated seismic reflection profiles SCREECH 1-IAM 11 (Ranero and Pérez-Gussinyé, 2010; Hopper et al., 2004), based on interpretations of observations (Boillot et al., 1987) and kinematic rules to thin the crust described in that work. Ranero and Pérez-Gussinyé (2010) suggested that faults (F1-F7, Fig. 1.b) were sequential in time and always formed in the hanging wall to the previous one, leading to progressive younging of faulting and syntectonic sediments towards the basin center and asymmetry formation. This oceanward sequential faulting mode has been broadly confirmed by recent 3D seismic data (Lymer et al., 2019). However, these data show that in three dimensions, groups of faults may be active simultaneously, especially when faults laterally merge. *For simplicity, we impose one active fault on the WIM and a small conjugate on the Newfoundland side at the same time.* These small faults appear in dynamic models that produce asymmetric margins (Andrés-Martínez et al., 2019), and relieve the deviatoric stress at Newfoundland side that would occur if only one fault was active (Fig. S1). The phenomena of oceanward deformation migration have also been reported at the southern segment of the rift systems (Péron-Pinvidic et al., 2013) and described by previous forward geodynamical modeling (Brune et al., 2014; Andrés-Martínez et al., 2019). The original fault dips range from 55°-65° and are interpreted from the angular relationship between the basement (black lines in Fig. 1.b) and the top of early synrift strata (blue line in Fig. 1.b). The kinematics of the last sequential fault, F7, which has a semi-horizontal appearance in the seismic profile (Fig. 1b), is not well constrained. For simplicity, we assumed F7 has the same original fault dip as F6.

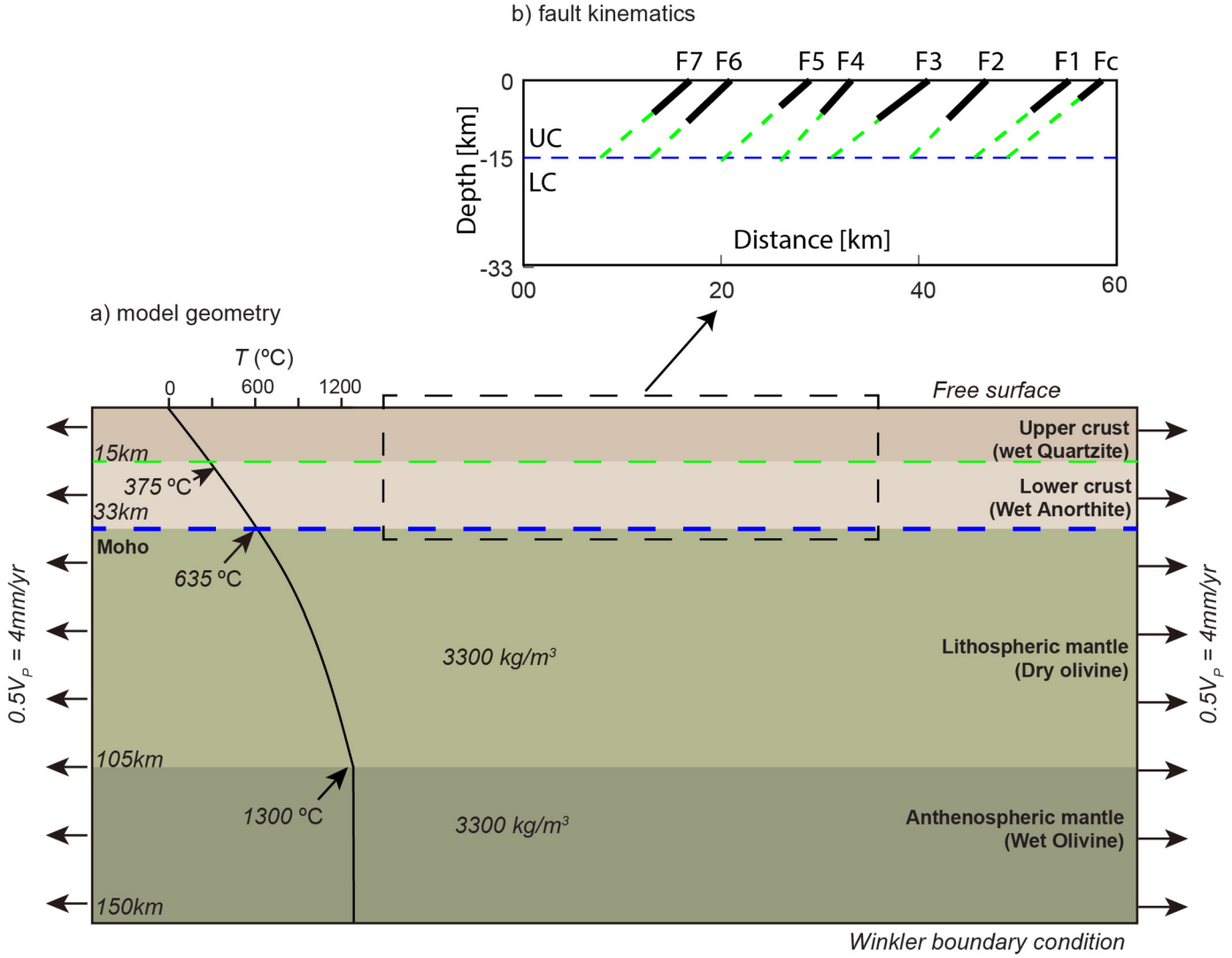

Fig. 2. Model setup. (a) A 2D model with initial 200 km wide and 150 km depth is used to simulate the evolution of WIM_NF margins. In the first-time step of the Basin stage, we impose a thermal weak seed at the model center which has a 2-D Gaussian shape. For the margin stage, we introduce weak fault zones to guide the simulation of localization of plastic deformation. (b) Fault kinematics that are imposed as weak seeds in the model. The length of black solid lines shows the expected fault offsets, and the green lines show the depth of weak zones.

The rheological properties of the lower crust and the Moho temperature are thought to have an important influence on rifting but cannot be well determined (e.g., Ros et al., 2017). Thus, we conducted additional tests to discuss those effects in the following section.

2.4. Sensitivity tests

We varied strength either by changing lower crustal composition from wet anorthite (Rybacki and Dresen, 2000) to weaker wet quartzite (Gleason and Tullis, 1995) (Fig. 3) or by updating Moho temperature (Fig. S2). Wet quartzite is used for the upper crust for all cases. The model with weaker wet quartzite lower crust (Fig. 3b) results in an array of upper crustal faults which present a shallower final fault dip angle and less crustal thinning than that with wet anorthite lower crust (Fig. 3a). This is because the weaker lower crust allows intense flow towards the tip of active faulting, which results in larger fault rotation and less crustal thinning (e.g. Whitney et al., 2013). It should be noted that to conduct this comparison, we run the code in fully dynamic mode with the same wet anorthite rheology up to the time at which we activate the kinematic-dynamic mode. It is only when we include the faults as weak planes that we change the lower crustal rheology. This is done to show only how different lower crustal rheologies respond to the same fault kinematic history.

We also ran a set of models with different initial Moho temperatures but the same lower crustal rheology (Fig. S2). The initial Moho temperature is varied by changing the lower crust radiogenic heat production. Pressure-temperature-time (P-T-t) paths of amphibolite from site 1067 ODP drilling (Gardien et al., 2001) give a range of temperatures of 500-770 °C for the pre-rift Moho. Hence, we tested three models with 550 °C, 635 °C and 750 °C as initial Moho temperatures, respectively. As the initial Moho temperature is increased, the Moho is flatter under the overlying rotated blocks (Fig. S2). For lower temperatures, the Moho undulates at fault block-scale, and becomes shallower under the deepest segments of the overlying faults (Fig. S2a and S2b). Concomitantly, with decreasing Moho temperatures, the lower crustal layer becomes thinner, but does not disappear under the overlying rotated blocks (Fig. S2a).

To ensure the robustness of the model presented here, additional tests have also been conducted. The results show that the numerical resolution (Fig. S3), as well as rate and magnitude of strain softening (Fig. S4), have only a negligible effect during the

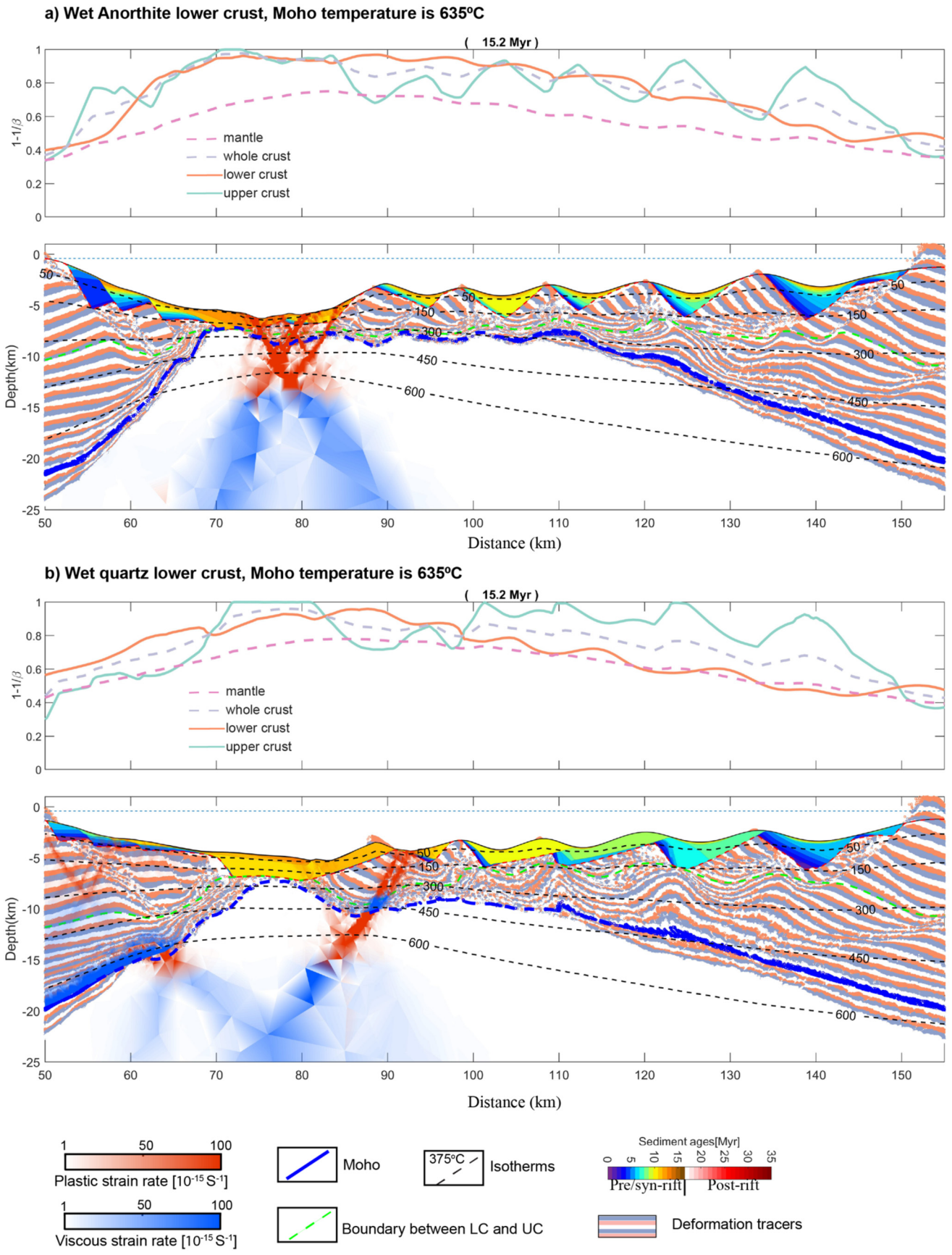

Fig. 3. Effect of varying lower crustal rheology on margin structure. Here we compare the result of kinematic-dynamic modelling using different rheologies. For this we use the same thermal structure, geometry configuration and fault kinematics for models, but different lower crustal rheologies: a) wet anorthosite rheology and b) wet quartzite rheology. The comparison between these models demonstrates that the observed margin architecture is only reproduced when the lower crust is relatively strong.

kinematic-dynamic simulation stage. Their effect is small because the plastic deformation of the upper crust in our model is mainly influenced by the kinematic fault that we have imposed. This is different from a pure forward model, where these parameters controlling the strain weakening are shown to have a significant effect on fault geometry (Lavier et al., 2000; Naliboff et al., 2017).

In the next paragraphs, we focus on the model that best fits the observations, which has a wet-anorthosite lower crust and a Moho temperature of 635 °C (Fig. 4). The final model configuration after 115 million years of evolution matches remarkably well the seismic section, including the tectonic asymmetry, the fault-block topography, the stratigraphic patterns, the spatial pattern of Moho shallowing, as well as the detachment geometry. The remarkable match between model and observations indicates that our parameter choice and the consequent model deformation are good candidates to reproduce the natural rift evolution. Although a slightly different parameter choice may also explain the evolution of deformation along the seismic lines, the similar deformation patterns of our coldest models (Fig S2a, b), which are the ones that best fit the seismic lines, indicates that our model results can shed light on some unresolved debates.

3. Model evolution

3.1. Evolution of brittle and ductile deformation

The early phases of evolution, the early basin stage, is ran in a 'dynamic' mode'. Extension is characterized by distributed faulting across the whole model (Fig. 5a). Horsts and grabens structurally form the basin with maximum subsidence of $\sim$ 500 m (Fig. 5a.1). Thinning in the upper, lower crust and mantle is similar, indicating uniform extension (Movie 1). With increasing extension (Fig. 5a.2), strain starts to localize in fewer larger faults/shear zones that propagate towards the crust base. As fault offset increases, the brittle faults/ductile shear zones jointly rotate to lower angles, 40°-35°, due to footwall unloading (Buck, 1988).

From 6.6 My onwards, we start to simulate the last stages of extension that led to break-up (the margin stage of Ranero and Pérez-Gussinyé, 2010) by imposing sequential faults Fc to F7. The first sequential fault, Fc, is not imaged along IAM11, but its presence is required to match the occurrence of early syn-rift sediments on IAM11, which are formed later in our model evolution (Fig. 5b.2 and 5b.3). The first clearly imaged fault along IAM11 is F1, which becomes active after Fc (the tectonic evolution of F1 is shown in Fig. S6). As F1 slips, lower crust exhumes along its footwall and cools. F1 is an entirely brittle structure throughout the upper crust at 8.1 Myr (Fig. 5b.1). However, at depth, it laterally juxtaposes cold and brittle anorthosite lower crust in its footwall side, with hotter and ductile wet quartzite upper crust in its hangingwall side (Fig. 5b.1). Thus, F1 bifurcates at depth into brittle faulting through the top of the colder, stronger lower crust and a low-angle ductile shear zone at the base of the upper crust (Fig. 5b.1). The bifurcation of deformation at depth also be observed in dynamic models with similar initial conditions, where no faults are prescribed (Fig. S7). However, this phenomenon has not been accurately evaluated because forward dynamic models have not been compared to data at fault-block scale and the effect of this secondary brittle branch of deformation has been overlooked.

The next sequential fault F2 exhibits the same pattern of deformation as F1 (Fig. 5b). As F2 slips, its footwall rigidly back-rotates affecting the deepest segment of F1 and contributing to the flattening of F1 at depth (Fig. 5b.2). As with previous faults, F2 pulls the lower crust towards its footwall, so that the crust becomes thinnest immediately below the deepest brittle segment of F2, where the upper crust is also thinnest (Fig. 5b.2). This deformation pattern repeats itself for each future sequential fault, so that the Moho acquires an undulating geometry with its shallowest parts located vertically beneath the footwalls of the faults, around where the upper crust is locally thinnest.

3.2. Formation of low-angle detachments

The new fault F3, located in F2's warm hangingwall, is brittle only in the uppermost upper crust and propagates as a ductile shear zone through the deepest upper crust and the lower crust (Fig. 6b.1). In our model, F3 corresponds to the breakaway of the S detachment along IAM11. For small offsets, the brittle and ductile parts of F3 rotate by similar amounts (Fig. 6b.2). As F3 continues to slip (Fig. 6b.3), it drags a large amount of lower crust into its footwall, resulting in a narrow channel of the lower crust in its hangingwall. With further thinning and unloading, the ductile shear zone that is the continuation of F3 at depth, rotates and is active at an angle, i.e. 25°, which is lower than its brittle counterpart (Fig. 6b.3). This shear zone follows the relatively flat base of the upper crust, which is weaker and easier to deform than the underlying lower crust and mantle (since wet quartzite is weaker than anorthite at same temperatures). To assess the effect of resolution, we ran a model with a higher resolution in the lower crust than in the model described here (Fig. S8). The differences are small, with the shear zone still running along the base of the upper crust at a low angle in the higher resolution model. The final slip angles along F3 are 44° and 25° for its brittle and deeper ductile segments, respectively (Fig. 6b.3). Remarkably, these are precisely the same angles as those measured from stratigraphic relationships in 3D seismic data for the breakaway of S (Lymer et al., 2019) (Fig. S9). The coincidence in activity angles was not forced a priori, as we only input the initial fault angle in the upper crust. Thus, the evolution shown here reproduces not only the final margin architecture but also appears to reproduce fault geometries during S formation.

Continuing slip on F3 laterally juxtaposes cold and brittle wet anorthite lower crust in its footwall side, with hotter and ductile wet quartzite upper crust in its hangingwall side (Fig. 6b.3). This results in that F3 bifurcates into brittle and ductile deformation at depth. The brittle deformation occurs where the lower crust has been extremely thinned so that brittle deformation reaches the Moho. Ductile deformation occurs in a localized shear zone that connects to deeper and weaker lower crust and Moho further oceanwards. Subsequent faults, F4-F7, follow the same deformation patterns (Fig. 5b). As each of them works, they back-rotate and further flatten the deepest segments of the previous slip structures, which worked as narrow shear zones above an extremely thinned lower crustal channel, of laterally varying thickness. These back-rotated shear zones consecutively form a sub-horizontal detachment-like structure, that spatially coincides with S detachment (Fig. 4).

3.3. Breakup and mantle exhumation

The last sequential fault that we interpret along the seismic profile IAM11 is F7 (Fig. 1b). This fault is interpreted to be broken up and completely back-rotated by the structures that led to mantle exhumation in the peridotite ridge (Pérez-Gussinyé, 2013). After simulating F7 in kinematic-dynamic mode, we let the model evolve dynamically to simulate continental breakup and post-rift evolution. Remarkably, the final breakup location, which is not chosen a priori, breaks through block B7 and leaves a part of F7 beneath the narrow margin and another in the wide margin (Fig. 5b.8). The deepest part of F7 in the narrow margin, coincides with the deep reflection in the Newfoundland margin interpreted as the contin-

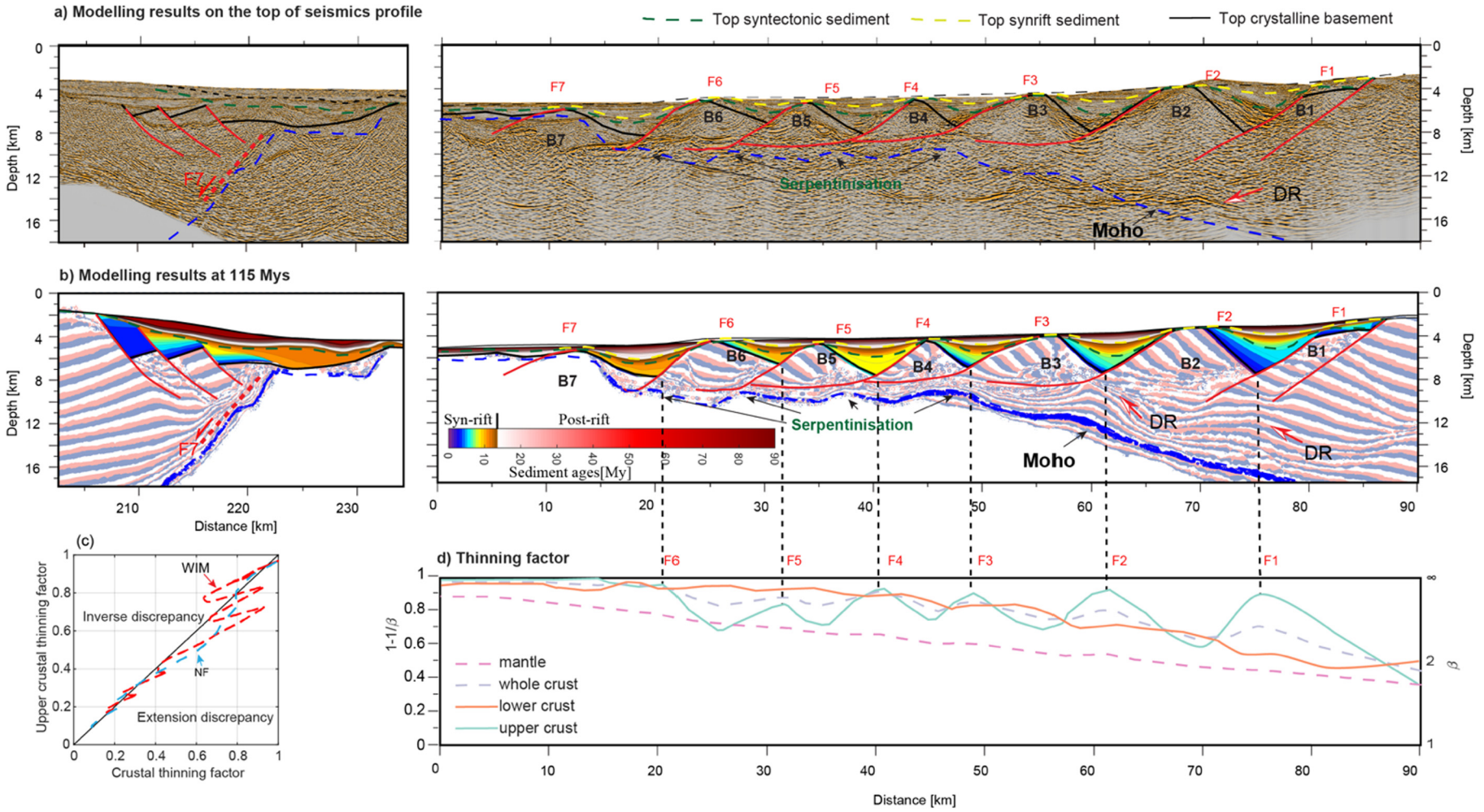

Fig. 4. Comparison between modelled results and observations. (a) Seismic section IAM11 overlain by the main modelled results, i.e. Moho, deformation planes (see (b)), basement geometry and the top of syn-tectonic, synrift and postrift sediments. DR marks deep reflectors. (b) Modelling result after 115 Myrs. F1-F7 and B1-B7 are major faults and fault blocks respectively. The red solid lines show deformation planes, defined as the axis of maximum total strain rate at the last time step each fault is active (Fig. S5). Dashed blue line shows the depth of modelled Moho. The DRs in the modelled section are the reflection of strong coupling between LC deformation and slip of overlying faults, indicating coupling of lower and upper crustal deformation. (c) Correlation plot of modelled UC thinning factor and whole crust thinning factor shows there is no large-scale crustal depth dependent stretching in the model. (d) Partition between LC and UC deformation shows UC and lower LC factors undulating around the whole crustal ones at fault-block scale, which indicates strong coupling between lower and upper crustal deformation. Thinning factors were estimated from thickness changes of crustal layers.

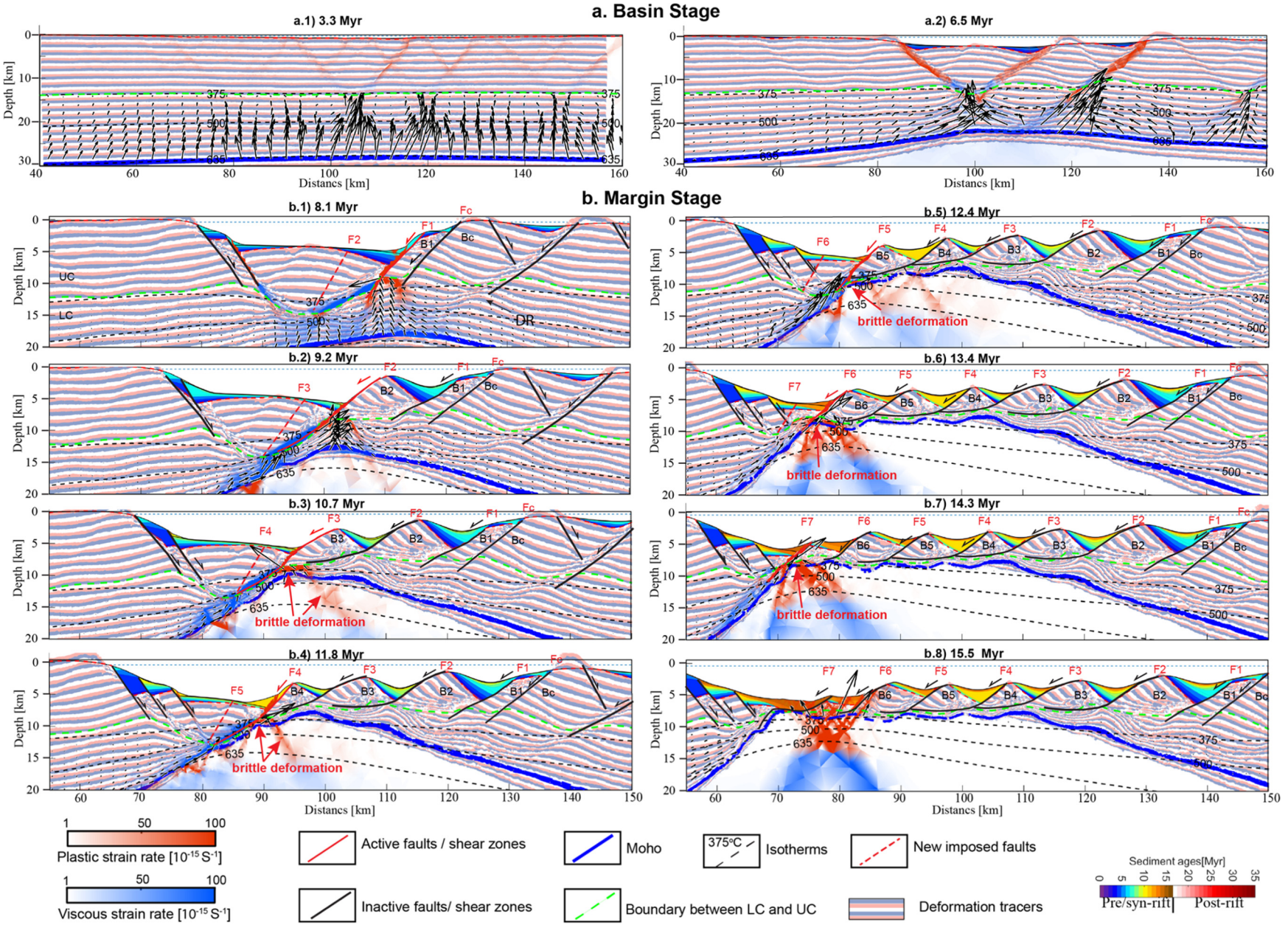

Fig. 5. Brittle and ductile evolution of the model showing development of margin asymmetry and the S detachment. (a) Modelled evolution during the basin stage. Black arrows show the lower crustal flow relative to the interface between lower crust and upper crust. The relative lower crustal flow towards the footwall of active faults, where crustal thinning is maximum, indicates strong coupling between lower and upper crustal deformation. (b) Stepwise kinematic-dynamic modelled evolution of the margin stage. With continuous crustal thinning, the brittle deformation in the footwall of sequential faults reaches the mantle (marked by red arrows in Fig. 1 b3-b7), brings water for mantle serpentinisation and produces some landward-dipping faults in the mantle as in seismic profile IAM11. Geometries of faults F1-F7 are measured from IAM11 (Fig. 1b) and are imposed sequentially to the model by introducing weak fault zones in the upper crust. See SI Movie S1 and S2 for a stepwise evolution.

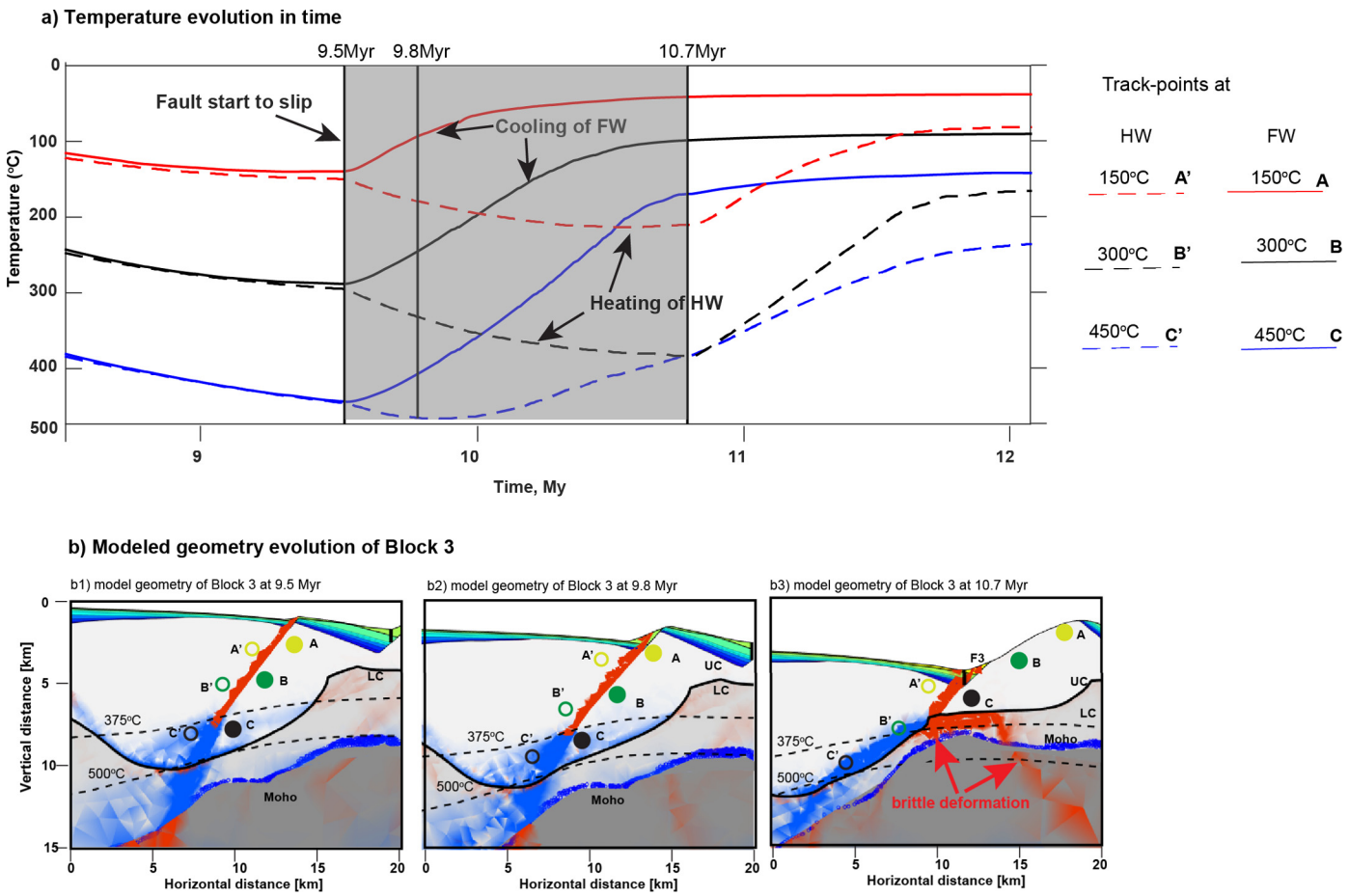

Fig. 6. Geometry and thermal evolution of fault F3. (a) Temperature evolution in time shows the different thermal history of tracers in the footwall (FT) and hanging wall (HW) of fault F3. The position of the tracers is shown in Fig. 6(b). The gray shaded region shows the time period when fault F3 slipped. (b) F3 starts at high angle, and as it slips, the fault planes rotate to lower angle due to hangingwall unloading. Continued slip on F3 exhumes and cools its footwall, resulting in lateral juxtaposition of cold and brittle lower crust in the footwall with hotter and ductile upper crust in the hangingwall during fault activity. Once fault F3 is inactive, new faults in its hangingwall back-rotate its deepest ductile segments and form a sub-horizontal detachment-like structure, such as "S". This process repeats itself in time and space for each new sequential fault, F4 to F7. Figure legend and color as in Fig. 5.

uation of F7 from the West Iberia margin (as had been earlier interpreted by Hopper et al., 2004; Pérez-Gussinyé, 2013) (Fig. 4).

4. Discussion

4.1. Lower crustal deformation

In our model, the lower crust is pulled up by the deep-penetrating slip structures and flows towards the faults' footwalls, as shown by black arrows in Fig. 5. This process thins the crust in the area of active faulting and generates local lower crust excesses in the footwalls relative to the hangingwalls. Therefore, it results in upper and lower crustal thinning factors that undulate around the whole crustal ones (Fig. 4). The flow of the lower crust towards the deepest overlying fault tips results in lower crustal deformation fabrics that follow the upper crust deformation (Fig. 7b). Similar fault-block scale variability in thinning factors (Pérez-Gussinyé et al., 2003) (Fig. 7a) and lower crustal deformation fabrics (Fig. 7b), which stand out as strong reflections in seismic profiles, are observed in margins worldwide, indicating the global predominance of coupling processes at magma-poor margins (Fig. 7) (Clerc et al., 2018; Osmundsen and Péron-Pinvidic, 2018; Pérez-Gussinyé et al., 2003).

Our results identified a contribution to the extension discrepancy measured from upper crustal faults and whole crustal thinning that was unrecognized by Reston and McDermott (2014). In our model, lower crust is dragged towards the fault footwalls and produces local undulations of the upper and lower crustal thinning factors at the fault block scale (Fig. 7a1). Thus, the upper crustal thinning factor is higher than the lower crust one at the footwall of any fault, and the opposite is true for its hangingwall. During the basin stage, the lower crust and upper crust stretching factors undulate at wavelengths coinciding with active fault spacing, above and below the total crustal stretching factors, indicating there is no large-scale differential thinning between them (Movie S1). Large faults reproduce these patterns during the margin stage but with a larger difference between the upper crust and lower crust stretching factors. With faults acting sequentially in time, this process reproduces itself and accumulates in time and space with each new fault, so that in the end, the lower crust appears to have been preferentially thinned from the most extended basin sector over a distance of ~30 km (faults F4 to F6, Fig. 4d). However, this preferential thinning is not the result of the large-scale flow of the lower crust. Instead, lower crust flow is local, reflecting the strong coupling between the upper crust and lower crust deformation. These results coincide with the interpretations from multichannel and wide-angle seismic data made by Pérez-Gussinyé et al. (2003) and Ranero and Pérez-Gussinyé (2010), who suggested that there was no large-scale differential extension of the upper and lower crust at magma-poor margins, and that differences in the amount of upper crustal and lower crustal thinning were local and driven by shear along upper crustal faults. Our results also coincide with

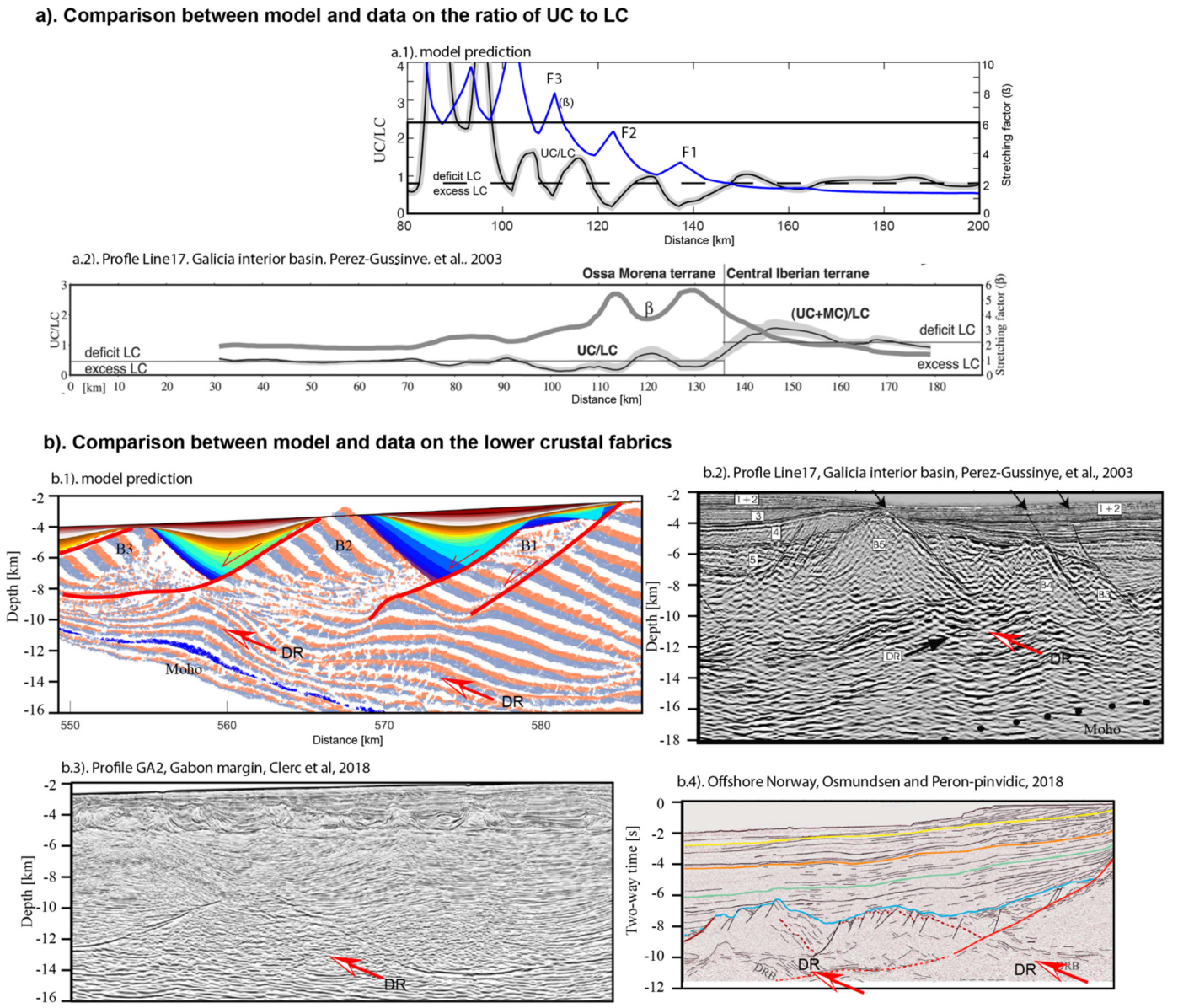

Fig. 7. a) Comparison between the modelled ratio between upper crustal (UC) thickness to lower crustal (LC) thickness, top, with the observed UC/LC ratio from Galicia interior Basin, bottom (Pérez-Gussinyé et al., 2003). **b)** Comparison between modelled lower crustal deformation fabrics and deep reflectors observed in margins worldwide at the same scale. (b.1) Modelling result at 115 Myrs, with legend and coloring as in Fig. 5. (b.2-b.4) strong reflectors in the lower crust from Galicia interior basin (Pérez-Gussinyé et al., 2003), Gabon margin (Clerc et al., 2018) and offshore Norway (Osmundsen and Péron-Pinvidic, 2018). Some studies have inferred that the deep reflectors offshore Norway represent magmatic underplating (e.g., Mjelde et al., 2002), but even so, the upward doming geometry may reflect tectonic deformation to some extent. The geometry of these crustal reflectors has been shaped by slip on overlying faults, indicating strong coupling of lower and upper crustal deformation at large extension factors.

those of Huismans and Beaumont (2011), who suggested that the lithospheric mantle would thin less than the whole crust at their so-called Type 1 margins (see Fig. 4d).

4.2. Temperature evolution across the active normal faults

One prediction of our model is that during extreme extension, rocks in the footwall of each active fault, cool, while those in their hangingwall heat. Fig. 6.a shows the temperature evolution curves of six tracers on the hangingwall and footwall of F3, at three different initial depths. These curves show that during faulting the footwall cooled, while its hangingwall warmed up (9.5-10.7 Myr. Fig. 6a). After fault slip, the temperature difference between two points that were at the same temperature at fault onset, one in the hangingwall and the other in the footwall, can reach up to 300 °C (see black tracer in Fig. 6a). Many studies have documented the cooling history of normal fault's footwalls during large displacement (e.g., Davis et al., 1986), but little has been reported to show that the hangingwall of the fault is heating at the same time. This may be due to the fault that the basement rocks in the hangingwall of the fault tend to be covered by thick sediments and are difficult to collect and study. Fortunately, in the hangingwall of the Rechnitz core complex at eastern Alps, vitrinite reflectance data of the early sediments reveals the heating history of the fault's hangingwall during slip (Dunkl et al., 1998).

The difference in temperature evolution between the two sides of an active fault is a function of fault offset and fault dip angle. The difference in temperature between the two sides of the fault becomes more pronounced as the fault offset is larger and the fault dip angle is steeper. Thus, the differential heating and cooling across the fault is only clearly observed when fault offsets are large as observed in seismic profiles. Previous models of asym-

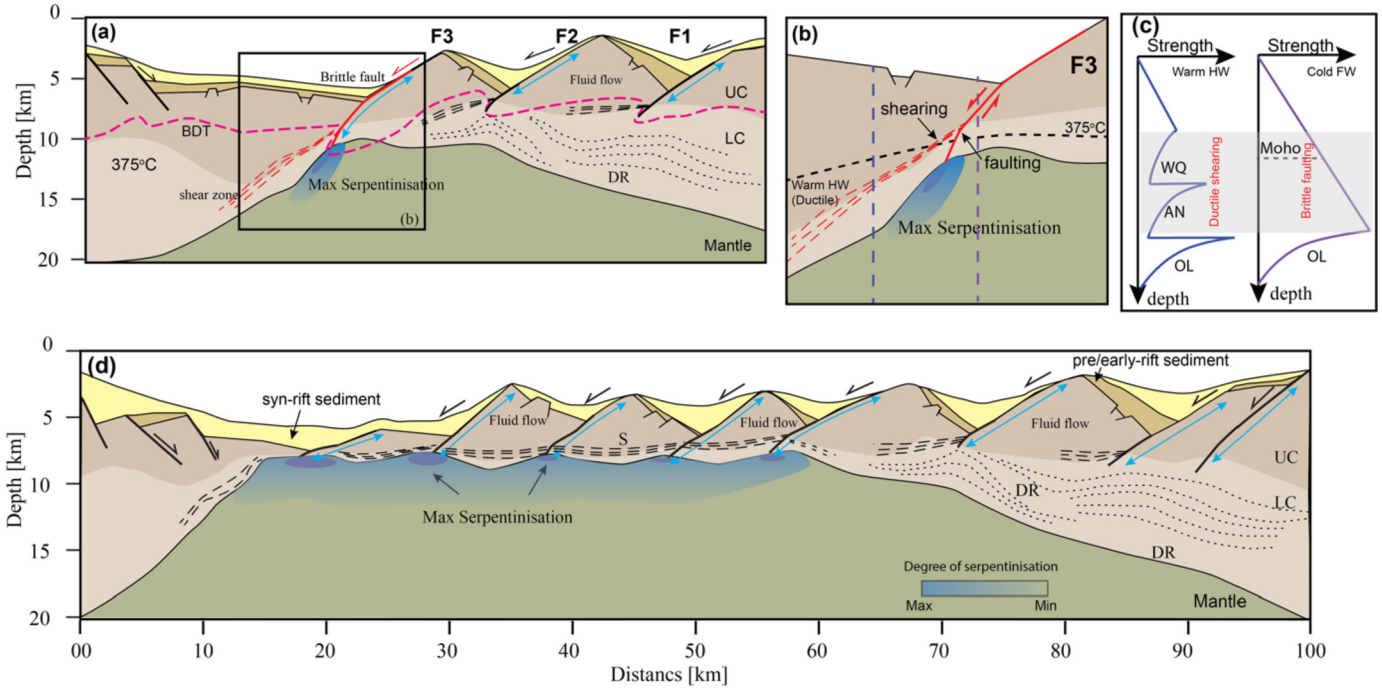

Fig. 8. Conceptual model of crustal thinning and detachment formation at magma-poor margins based on kinematic-dynamic modelling. (a) Strong coupling between brittle and ductile deformation with increasing extension results in flow of LC, from the hangingwalls, HW, towards the footwalls, FW, of faults, and formation of gently dipping LC deformation fabrics, DR (as shown in dotted lines). BDT represents the brittle-ductile transition at the time when each of the faults was active. During each fault activity, the BDT is deeper in the FW than in the HW. (b) Slip on a fault progressively exhumes and cools its FW and leads to HW heating, allowing across-fault variation in brittle faulting in the FW (solid lines) and ductile shearing in the HW (dashed lines). Ductile shearing in the HW leads to low angle slip, ~25°, along the developing detachment, and brittle faulting in the FW provides water for mantle serpentinisation. c) Representative strength profiles across active faults F3-F6, showing brittle behavior in the FW and ductile in the HW. (d) Each narrow ductile shear zone is later back rotated to sub-horizontal by new oceanward sequential faults to form the S reflector. Maximum serpentinisation is located where brittle faults intersect S, as in Bayrakci et al., 2016. Blue shading indicates serpentinisation degree increasing from light to dark.

metric extension have comparatively smaller fault size in the distal margin domains than the one presented here, and have overlooked this effect (Brune et al., 2014). The different thermal evolution across each normal fault, in combination with different lithologies between upper and lower crust, results in coexisting ductile and brittle deformation at depth, which is key to understand magma-poor margin configuration as explained in the following section.

4.3. S detachment and its relationship to margin asymmetry and mantle hydration

In our model, each active, upper crustal fault bifurcates at depth into two branches of brittle and ductile deformation because of cooling of the fault's footwall and heating of its hangingwall. Brittle deformation in the footwalls reaches the Moho and explains mantle serpentinization at the propagation in depth of the overlying faults. On the other hand, deformation along localized, ductile shear zones, which are subsequently back rotated by future new oceanward faults, explains the formation of detachment-like structures such as *S* observed at many magma-poor margins worldwide (Fig. 8). Thus, the so-called *S* detachment is the culmination of an asymmetry formation process through sequential faulting and lateral rift migration that started earlier in the margin history (Ranero and Pérez-Gussinyé, 2010) and not the cause of final conjugate asymmetry (Lymer et al., 2019).

In our model the crust is not completely brittle before detachment formation, as suggested previously (Lymer et al., 2019; Pérez-Gussinyé and Reston, 2001). Progressive cooling due to ultra-slow extension is essential in the fault footwalls but not in their hangingwalls, where the deepest upper crustal and lower crustal levels become progressively hotter and more ductile (Fig. 8). Thus, in our model S is formed by the continuation at depth of the overlying brittle faults into discrete shear zones which laterally merge. These shear zones slip at low-angle, 20°-25°, as indicated by stratigraphic relationships in seismic data (Fig., S8, Lymer et al., 2019) and become sub-horizontal as they are rotated by younger, oceanward faults. Therefore, S is a composite structure, in accord with the observation that corrugations are continuous from the overlying faults to the *S* reflector in 3D seismic data (Lymer et al., 2019), but was not formed in the brittle field as earlier proposed (Pérez-Gussinyé and Reston, 2001; Lymer et al., 2019).

This result implies that some highly thinned and strongly deformed lower crust may remain beneath S. Its thickness laterally varies and ranges between hundreds of meters to 1-1.5 km at most for our two best fit models (Fig. S2a, b). Thus, it is probably too thin to be resolved by travel-time analysis of wide-angle data. The observed seismic velocity immediately below S varies across a broad range of values that have been interpreted as representing varying degrees of serpentinisation (Bayrakci et al., 2016; Schuba et al., 2018). In some places velocities are also consistent with those of the lower crust in less extended areas nearby (Pérez-Gussinyé et al., 2003; Zelt et al., 2003). Since the mantle underneath the extremely thinned lower crust is also serpentinised, there might be no impedance contrast at the base of such thin, lower crustal fragments, as observed in the wide-angle data. The model fits geological observations of the Err detachment (Manatschal and Nievergelt, 1997), located in the distal sections of the ancient Tethys margins now exposed in the Alps, which show that the middle Err was intra-crustal.

Finally, the results reveal the potential tectonic paths of water influx into the mantle at magma-poor rifted margins. During extreme extension, the brittle deformation in the footwalls of active upper crustal faults is more effective at crustal thinning, so that at these locations, the crust becomes extremely thin, and brittle deformation reaches the Moho. This is where the mantle is

also colder (Fig. 5 and Fig. 6), and where maximum water penetration through brittle faults and serpentinization may have occurred (Fig. 4b, Fig. 8). This result is consistent with evidence from 3D wide-angle data that shows that maximum serpentinization occurs where brittle faults overlying S intersect the detachment (Bayrakci et al., 2016), and provides a framework to study paleo hydrothermal systems related to mantle hydration, which fuel chemosynthetic life in these deep and cold environments (Albers et al., 2021).

5. Conclusions

To identify controls on the asymmetry, modes of deformation, and mantle hydration that characterize the distal sections of magma-poor margins, we use a forward modelling technique that combines thermo-mechanical models of rifting with fault kinematics inferred from high resolution seismic profile. This approach allows us to determine a model evolution which, although non-unique, is consistent with the laws of rock deformation and with the fault-block-scale tectonic structure observed along the West Iberia-Newfoundland margins. Our model results indicate that an interpretation where faults work sequentially in time can reproduce the observed crustal thinning profiles and conjugate margin asymmetry. In addition, they show that during deformation there is no large-scale differential stretching of the upper and lower crust.

Our model shows that during extreme extension, rocks in the footwall of each active fault, cool, while those in their hangingwall heat. The heating of the hangingwall allows the crust to warm sufficiently for ductile deformation to take place at relatively shallow crustal levels. This results in that each high-angle, upper crustal fault, connects to a low-angle (20-25°), ductile, narrow shear zone, which localizes deformation from the base of the upper crust to the lower crust and mantle. When a new oceanward, high-angle, upper-crustal fault forms at the hangingwall of the last active fault, its footwall rotation further flattens the ductile shear zone. This process repeated in time and space leads to the formation of a detachment-like structure in the distal margin areas. Simultaneously, the cooling of the footwall explains the mantle hydration through brittle deformation. The result suggests that the shallow-dipping S reflector, commonly referred to as a detachment in seismic sections, does not mark a single brittle structure that slipped consistently along its entire length, but a composite ductile shear zone activated segment-by-segment as upper crustal faulting migrated oceanward. Detachment formation would thus be a byproduct and not a root cause of margin asymmetry. The numerical models also predict variations in upper/lower crustal thickness on wavelengths that coincide with fault spacing, consistent with thinning factors calculated at real margins.

This study allowed us to reveal with unprecedented detail, the tectono-thermal history of a magma-poor margin. Thus, the model provides a quantitative framework to study hydrothermal systems related to serpentinization during extreme extension, their associated hydrogen, methane production, and the chemosynthetic life they sustain.

CRediT authorship contribution statement

Z.L. performed the thermo-mechanical model simulations, did the post-processing and figures. M.P.G. and Z.L. interpreted the simulations, designed and wrote the draft of the paper. L.R., T.A.M. and G.B. contributed to the discussions, improvement of text and Figures. I.M. contributed to modelling techniques. M.P.G. and L.R. designed and wrote the project leading to this research.

Declaration of competing interest

The authors declare that they have no known competing financial interests or personal relationships that could have appeared to influence the work reported in this paper.

Acknowledgements

We thank Javier Garcia-Pintado, Roger Buck and Leila Mezri for feedback on the earlier version of the manuscript. Suggestions by John Naliboff and an anonymous reviewer improved this paper. This work was supported by German Research Foundation Grant (DFG) 396827560. The numerical method used here has been described in detail in Muldashev (2021). The input file, fault kinematic table and original model output data for this study can be found at: https://doi.org/10.5281/zenodo.5598088.

Appendix A

A.1. Forward geodynamical numerical methods

A.1.1. Governing equations

KinDyn is a 2D lithosphere extension numerical code, originally based on MILAMIN (Dabrowski et al., 2008), a finite element method to solve the equation of mass, momentum and energy conservation. MILAMIN has been extended to include nonlinear visco-elastic-plastic behavior, a free-surface, strain softening (Ros et al., 2017) and Winkler bottom boundary condition and surface processes (Andrés-Martínez et al., 2019). Deformation and pressure are calculated by solving Stokes force-balance equation:

$$\nabla \cdot \tau - \nabla \mathrm{P} + \rho g = 0 \tag{1}$$

where τ is deviatoric stress, P the total pressure, ρ the density and g the gravitational acceleration, and mass conservation equation:

$$\nabla \cdot v = 0 \tag{2}$$

where v is velocity. Temperature is estimated by solving the energy conservation equation:

$$\rho C_P \cdot \frac{DT}{Dt} = \nabla \cdot (k \nabla T) + H_0 + H_S \tag{3}$$

where C_P is the effective heat capacity, T is the temperature, t is the time, k is the thermal conductivity, H_0 is the crustal radioactive heat production, and H_S is shear heating production that depends on stress and strain rate.

A.2. Rock rheology models

Visco-elasto-plastic rheology is implemented in our model. This is achieved by adopting an additive decomposition of the deviatoric strain rate into elastic, viscous and plastic components. The relation between shear stress τ and effective viscosity η_{eff} described as:

$$\tau = \eta_{eff} \cdot 2\dot{\varepsilon} \tag{4}$$

where $\dot{\varepsilon}$ the deviatoric strain rate. In order to estimate the effective viscosity, the Drucker-Prager yield equation is adopted to evaluate whether the material deforms plastically or visco-elastically. Plastic deformation dominates the model when the second invariant of deviatoric stress σ_{II}, is larger than the plastic yield stress σ_{yield}, which defined as:

$$\sigma_{yield} = P sin\varphi + C cos\varphi \tag{5}$$

where C is the cohesion of the rocks and φ is the frication angle. To include plasticity into the viscous formulation, the effective viscosity η_{eff} of yielding material is defined as:

$$\eta_{eff} = \frac{\sigma_{yield}}{2\dot{\varepsilon}_{II}} \tag{6}$$

where $\dot{\varepsilon}_{II}$ is the square root of the second invariant of strain rate. When $\sigma_{\mathrm{II}} < \sigma_{yield}$, the material behaves visco-elastically, and we describe effective viscosity η_{eff} as:

$$\frac{1}{\eta_{eff}} = \left(\frac{1}{\eta_{dis}} + \frac{1}{\eta_{dif}} + \frac{1}{\mu \Delta t}\right) \tag{7}$$

where η_{dis} is the dislocation creep viscosity, η_{dif} is the diffusion creep viscosity, μ is the shear modulus and Δt is the numerical time step. The creep flow is described by nonlinear power-law temperature- and stress-dependent rheologies as:

$$\eta_{dis/dif} = \mathrm{B}^{-\frac{1}{n}} \dot{\varepsilon}_{II}^{\frac{1-n}{n}} exp\left(\frac{E + PV}{nRT}\right) \tag{8}$$

where B is the pre-exponential factor of the flow law, n is the power-law exponent, E is the activation energy, and V is the activation volume, R is the gas constant, and T is the absolute temperature.

A.3. Sediment transport models

The sediment transport due to erosion and sedimentation is simulated by assuming that the change in surface elevation rate is equal to the divergence of the sediment flux (Andrés-Martínez et al., 2019, Pérez-Gussinyé et al., 2020) plus a source term, S. The equation is therefore:

$$\frac{\partial h}{\partial t} = \frac{\partial}{\partial x}(K\frac{\partial h}{\partial x}) + S \tag{9}$$

where h is the topography, K is the diffusivity of the sediments, x is the horizontal direction and S is an additional sediment deposition source. K varies depending on whether the model top is in subaerial or submarine conditions.

When sediments are above sea-level, K is described as:

$$K = K_L + kax_d \tag{10}$$

where K_L subaerial diffusion coefficient, α is the transport coefficient and x_d is the distance from topographic highs to drainage divide.

When sediments are below sea level, K is estimated as:

$$K = K_s e^{(-\lambda_s h_w)} \tag{11}$$

where K_S submarine diffusion coefficient, λ_s is the submarine diffusion decay coefficient and h_w is the water depth. Additional sediment S includes not only pelagic sources but also sediment from a third, lateral dimension, making this what is sometimes referred to as a 2.5-dimensional model. This additional sedimentation rate S is a function of water depth as described:

$$S = C_s h_w^* \tag{12}$$

where Cs is a constant value and h_w^* is the high-pass filtered water-depth, which is found by subtracting the low-pass water-depth with wave numbers > $(\pi/30)$ km from the raw water-depth profile along with the model. In this way, the additional sediments are expected to deposit at local grabens. The thermal conductivity and density of sediments are the same as those of the underlying upper crust. The thermal effect of sedimentation on deformation has been discussed at length in a previous study (Andrés-Martínez et al., 2019). Erosion and sedimentation parameters used in the models are shown in Table S1. These parameters are chosen so that the modelled sediment architecture simulates that observed along our target seismic profile.

A.4. Weakening mechanisms

We introduced two mechanical weakening mechanisms to simulate strain localization, namely plastic strain softening and vicious strain softening. Plastic strain softening is achieved by decreasing the friction coefficient with increasing accumulated plastic strain. An initial friction angle of 30° (friction coefficient of 0.577) is linearly reduced to 15° (friction coefficient of 0.268) for the accumulated plastic strain of 1. For plastic strain exceeding 1, the friction coefficient remains constant at 0.268. Viscous strain softening is implemented by linearly increasing the pre-exponential factor B of the dislocation creep law (Eq. (8)) with the viscous accumulated strain (Andrés-Martínez et al., 2019). The viscous strain-softening mechanism simulates the effects of reducing grain size caused by large strains, possibly via dislocation creep and dynamic recrystallization. Also, viscous strain softening is reduced in the temperature range of 800° to 1200° Celsius with the Arrhenius function and ruled out in higher temperatures (see Ros et al., 2017). The effect of serpentinization induced weakening is not included in this study since it remains unclear which assumption should be preferred to model serpentinization at large scale. For example, some studies (e.g., Lavier and Manatschal, 2006) relate serpentinization to shear deformation, whereas other studies (Rüpke and Hasenclever, 2017) used a temperature-dependent law derived from experiments of olivine powder hydration.

Appendix B. Supplementary material

Supplementary material related to this article can be found online at https://doi.org/10.1016/j.epsl.2021.117288.

References

Albers, E., Bach, W., Pérez-Gussinyé, M., McCammon, C., Frederichs, T., 2021. Serpentinization-driven H2 production from continental break-up to mid-ocean ridge spreading: unexpected high rates at the West Iberia margin. Front. Earth Sci. 9, 673063.

Andrés-Martínez, M., Pérez-Gussinyé, M., Armitage, J., Morgan, J.P., 2019. Thermomechanical implications of sediment transport for the architecture and evolution of continental rifts and margins. Tectonics 38, 641–665.

Artemieva, I.M., 2006. Global 1× 1 thermal model TC1 for the continental lithosphere: implications for lithosphere secular evolution. Tectonophysics 416, 245–277.

Aydoğdu, A., Carrassi, A., Guider, C.T., Jones, C.K.T., Rampal, P., 2019. Data assimilation using adaptive, non-conservative, moving mesh models. Nonlinear Process. Geophys. 26, 175–193.

Axen, G.J., Karner, G., 2004. Mechanics of low-angle normal faults. In: Rheology and Deformation of the Lithosphere at Continental Margins, pp. 46–91.

Bannister, R., 2017. A review of operational methods of variational and ensemble-variational data assimilation. Q. J. R. Meteorol. Soc. 143, 607–633.

Baumann, T., Kaus, B.J., 2015. Geodynamic inversion to constrain the non-linear rheology of the lithosphere. Geophys. J. Int. 202, 1289–1316.

Bayrakci, G., Minshull, T.A., Sawyer, D.S., Reston, T.J., Klaeschen, D., Papenberg, C., Ranero, C., Bull, J.M., Davy, R.G., Shillington, D.J., 2016. Fault-controlled hydration of the upper mantle during continental rifting. Nat. Geosci. 9.

Blaich, O.A., Faleide, J.I., Tsikalas, F., 2011. Crustal breakup and continent-ocean transition at South Atlantic conjugate margins. J. Geophys. Res., Solid Earth 116.

Boillot, G., Recq, M., Winterer, E., Meyer, A., Applegate, J., Baltuck, M., Bergen, J., Comas, M., Davies, T., Dunham, K., 1987. Tectonic denudation of the upper mantle along passive margins: a model based on drilling results (ODP leg 103, western Galicia margin, Spain). Tectonophysics 132, 335–342.

Brune, S., Heine, C., Pérez-Gussinyé, M., Sobolev, S.V., 2014. Rift migration explains continental margin asymmetry and crustal hyper-extension. Nat. Commun. 5, 4014.

Buck, W.R., 1988. Flexural rotation of normal faults. Tectonics 7, 959–973.

Buck, W.R., 1991. Modes of continental lithospheric extension. J. Geophys. Res. 96, 20161–20178.
Clerc, C., Ringenbach, J.-C., Jolivet, L., Ballard, J.-F., 2018. Rifted margins: ductile deformation, boudinage, continentward-dipping normal faults and the role of the weak lower crust. Gondwana Res. 53, 20–40.
Dabrowski, M., Krotkiewski, M., Schmid, D., 2008. MILAMIN: MATLAB-based finite element method solver for large problems. Geochem. Geophys. Geosyst. 9.
Davis, G.A., Lister, G.S., Reynolds, S.J., 1986. Structural evolution of the Whipple and South Mountains shear zones, southwestern United States. Geology 14, 7–10.
Dunkl, I., Grasemann, B., Frisch, W., 1998. Thermal effects of exhumation of a metamorphic core complex on hanging wall syn-rift sediments: an example from the Rechnitz Window, Eastern Alps. Tectonophysics 297, 31–50.
Gardien, V., Poupeau, G., Muceku, B., Hébert, R., Beaudoin, G., Labrin, E., 2001. The evolution of amphibolites from site 1067, ODP leg 173 (Iberia Abyssal Plain): Jurassic rifting to the Pyrenean compression. Geol. Soc. (Lond.) Spec. Publ. 187, 191–208.
Gleason, G.C., Tullis, J., 1995. A flow law for dislocation creep of quartz aggregates determined with the molten salt cell. Tectonophysics 247, 1–23.
Hopper, J.R., Funck, T., Tucholke, B.E., Larsen, H.C., Holbrook, W.S., Louden, K.E., Shillington, D., Lau, H., 2004. Continental breakup and the onset of ultraslow seafloor spreading off Flemish Cap on the Newfoundland rifted margin. Geology 32, 93–96.
Huismans, R., Beaumont, C., 2011. Depth-dependent extension, two-stage breakup and cratonic underplating at rifted margins. Nature 473, 74–78.
Lavier, L.L., Manatschal, G., 2006. A mechanism to thin the continental lithosphere at magma-poor margins. Nature 440, 324.
Lavier, L.L., Buck, W.R., Poliakov, A.N., 2000. Factors controlling normal fault offset in an ideal brittle layer. J. Geophys. Res. 105, 431–442.
Lister, G., Etheridge, M., Symonds, P., 1991. Detachment models for the formation of passive continental margins. Tectonics 10, 1038–1064.
Lorenc, A.C., 1986. Analysis methods for numerical weather prediction. Q. J. R. Meteorol. Soc. 112, 1177–1194.
Lymer, G., Cresswell, D.J., Reston, T.J., Bull, J.M., Sawyer, D.S., Morgan, J.K., Stevenson, C., Causer, A., Minshull, T.A., Shillington, D.J., 2019. 3D development of detachment faulting during continental breakup. Earth Planet. Sci. Lett. 515, 90–99.
Manatschal, G., Nievergelt, P., 1997. A continent-ocean transition recorded in the Err and Platta nappes (Eastern Switzerland). Eclogae Geol. Helv. 90, 3–28.
Mjelde, R., Kasahara, J., Shimamura, H., Kanmimura, A., Kanazawa, T., Kodaira, S., Raum, T., Shiobara, H., 2002. Lower crustal seismic velocity-anomalies; magmatic underplating or serpentinised peridotite? Evidence from the Vøring Margin, NE Atlantic. Mar. Geophys. Res. 23, 169–183.
Muldashev, I.A., Pérez-Gussinyé, M., de Araújo, M.N.C., 2021. KineDyn: thermomechanical forward method for validation of seismic interpretations and investigation of dynamics of rifts and rifted margins. Phys. Earth Planet. Inter. 106748.
Naliboff, J.B., Buiter, S.J., Péron-Pinvidic, G., Osmundsen, P.T., Tetreault, J., 2017. Complex fault interaction controls continental rifting. Nat. Commun. 8, 1–9.
Osmundsen, P., Péron-Pinvidic, G., 2018. Crustal-scale fault interaction at rifted margins and the formation of domain-bounding breakaway complexes: insights from offshore Norway. Tectonics 37, 935–964.
Pérez-Gussinyé, M., Reston, T.J., 2001. Rheological evolution during extension at nonvolcanic rifted margins: Onset of serpentinization and development of detachments leading to continental breakup. J. Geophys. Res., Solid Earth 106, 3961–3975.
Pérez-Gussinyé, M., Ranero, C.R., Reston, T.J., Sawyer, D., 2003. Mechanisms of extension at nonvolcanic margins: evidence from the Galicia interior basin, West of Iberia. J. Geophys. Res., Solid Earth 108.
Pérez-Gussinyé, M., 2013. A tectonic model for hyperextension at magma-poor rifted margins: an example from the West Iberia-Newfoundland conjugate margins. Geol. Soc. (Lond.) Spec. Publ. 369, 403–427.
Pérez-Gussinyé, M., Andrés-Martínez, M., Araújo, M., Xin, Y., Armitage, J., Morgan, J.P., 2020. Lithospheric strength and rift migration controls on synrift stratigraphy and breakup unconformities at rifted margins: examples from numerical models, the Atlantic and South China Sea margins. Tectonics 39 (12), e2020TC006255.
Péron-Pinvidic, G., Manatschal, G., Osmundsen, P.T., 2013. Structural comparison of archetypal Atlantic rifted margins: a review of observations and concepts. Mar. Pet. Geol. 43, 21–47.
Peron-Pinvidic, G., Naliboff, J., 2020. The exhumation detachment factory. Geology 48 (6), 635–639.
Ranero, C.R., Pérez-Gussinyé, M., 2010. Sequential faulting explains the asymmetry and extension discrepancy of conjugate margins. Nature 468, 294–299.
Reston, T., 1996. The S reflector West of Galicia: the seismic signature of a detachment fault. Geophys. J. Int. 127, 230–244.
Reston, T., 2009. The structure, evolution and symmetry of the magma-poor rifted margins of the North and Central Atlantic: a synthesis. Tectonophysics 468, 6–27.
Reston, T., McDermott, K., 2014. An assessment of the cause of the 'extension discrepancy' with reference to the West Galicia margin. Basin Res. 26, 135–153.
Ros, E., Pérez-Gussinyé, M., Araújo, M., Romeiro, M.T., Andrés-Martínez, M., Morgan, J.P., 2017. Lower crustal strength controls on melting and serpentinization at magma-poor margins: potential implications for the South Atlantic. Geochem. Geophys. Geosyst.
Rüpke, L.H., Hasenclever, J., 2017. Global rates of mantle serpentinizationand H_2 productionat oceanic transform faults in 3-D geodynamic models: serpentinisation at transform faults. Geophys. Res. Lett. 44.
Reuber, G.S., Kaus, B.J., Popov, A.A., Baumann, T.S., 2018. Unraveling the physics of the Yellowstone magmatic system using geodynamic simulations. Front. Earth Sci. 6, 117.
Rybacki, E., Dresen, G., 2000. Dislocation and diffusion creep of synthetic anorthite aggregates. J. Geophys. Res., Solid Earth 105, 26017–26036.
Sandiford, D., Brune, S., Glerum, A., Naliboff, J., Whittaker, J.M., 2021. Kinematics of footwall exhumation at oceanic detachment faults: solid-block rotation and apparent unbending. Geochem. Geophys. Geosyst. e2021GC009681.
Schuba, C.N., Gray, G.G., Morgan, J.K., Sawyer, D.S., Shillington, D.J., Reston, T.J., Bull, J.M., Jordan, B.E., 2018. A low-angle detachment fault revealed: three-dimensional images of the S-reflector fault zone along the Galicia passive margin. Earth Planet. Sci. Lett. 492, 232–238.
Sibuet, J.C., Srivastava, S., Manatschal, G., 2007. Exhumed mantle-forming transitional crust in the Newfoundland-Iberia rift and associated magnetic anomalies. J. Geophys. Res., Solid Earth 112.
Whitney, D.L., Teyssier, C., Rey, P., Buck, W.R., 2013. Continental and oceanic core complexes. Geol. Soc. Am. Bull. 125, 273–298.
Zelt, C.A., Sain, K., Naumenko, J.V., Sawyer, D.S., 2003. Assessment of crustal velocity models using seismic refraction and reflection tomography. Geophys. J. Int. 153, 609–626.
Zhou, Q., Liu, L., 2017. A hybrid approach to data assimilation for reconstructing the evolution of mantle dynamics. Geochem. Geophys. Geosyst. 18, 3854–3868.